Active cancellation of power supply ripple effects in continuous wave superconducting radio frequency cavities

Feng Qiu[1,2], Takako Miura[1,2], Toshihiro Matsumoto[1,2], Shinichiro Michizono[1,2], Hiroaki Katagiri[1], Dai Arakawa[1], Hiromitsu Nakajima[1]

Abstract

Digital low-level radio-frequency (LLRF) systems are used at the compact energy recovery linac (cERL) test facility to stabilize the accelerating field inside the radio frequency (RF) cavities. Proportional and integral feedback controllers are implemented in the LLRF system to suppress the various disturbances in the cavities. At cERL, the typical disturbances include microphonics detuning and high-voltage power supply (HVPS) ripples. These two types of disturbances are reflected in the sum of sinusoidal fluctuations in the RF phase. Recently, a real-time narrow-band active noise control (ANC) approach which aims to reject the microphonics detuning of less than several dozen Hz, was proved to be effective in cavity resonance control. We extend this ANC method to the LLRF field control to suppress the RF ripples caused by the HVPS. In this paper, we present our experience of applying the ANC algorithm to the LLRF system of the cERL facility at KEK. We confirmed that high frequency ripples of up to 20 kHz can be well compensated by the ANC method during the cERL beam-commissioning.

Keywords: LLRF, Active noise control, cERL, HVPS ripple

[1]High Energy Accelerator Research Organization, 1–1 Oho, Tsukuba, Ibaraki 305–0801, Japan

[2]The Graduate University for Advanced Studies, Shonan Village, Hayama, Kanagawa 240–0193, Japan

1. Introduction

Field-programmable gate array (FPGA)-based digital low-level radio-frequency (LLRF) systems have been widely employed to regulate and control the accelerating field in various facilities such as the compact energy recovery linac (cERL) at KEK. The cERL is a 1.3 GHz superconducting (SC) radio-frequency (RF) test machine that is operated in continuous-wave (CW) mode [1, 2]. As shown in Fig. 1, a total of six cavities have been installed in the cERL. The injector consists of one normal conducting buncher cavity and three SC two-cell cavities (CAV1, CAV2 and CAV3). The other two nine-cell SC cavities (ML 1 and ML2) are installed in the main linac (ML). Various RF sources including two types of klystrons and two types of solid state amplifiers (SSAs) have been adopted in the cERL. A 25 kW klystron is used to drive the CAV1, while another 300 kW klystron is used to drive the CAV2 and CAV3 with vector-sum (VS) control. The SSAs serve as the RF sources for the cavities in the ML.

In the ML of the cERL, the cavities are operated with a high loaded Q (Q_L) of approximately 1.0×10^7, with a corresponding half-bandwidth of 65 Hz. The low cavity bandwidth makes the RF field very sensitive to the microphonics detuning [3]. The proportional and integral (PI) feedback (FB) controller is not sufficient to suppress the microphonic effects in our case. In view of this situation, we integrated a disturbance observer (DOB)-based control algorithm into the FB loops to speed up the system response to the microphonics. The experimental results confirmed that the microphonics detuning was well compensated by the "PI+DOB" control [2]. The cavities in the injector are operated with a lower Q_L compared with the cavities in the ML. The value of Q_L is approximately 1.2×10^6 for CAV1 and 0.5×10^6 for CAV2 and CAV3. The ripples in the klystron HVPS modulate the phase of the klystron output and ultimately lead to a phase modulation of the RF field in the cavity [4]. In the high voltage power supply (HVPS) of the 300 kW klystron, a ripples signal of approximately 300 Hz is observed. The corresponding 300 Hz component in the RF phase of CAV2 and CAV3 can be well suppressed by the "PI+DOB" control. However, a 20 kHz ripple exists in the HVPS of the 25 kW klystron. Although this component will be attenuated due to the low-pass characteristic of the cavity, it still limits the phase stability that can be achieved in CAV1. This component cannot be sufficiently suppressed by the large PI gains, since the large gains not only increase the risk of an unstable system but also deteriorate the high-

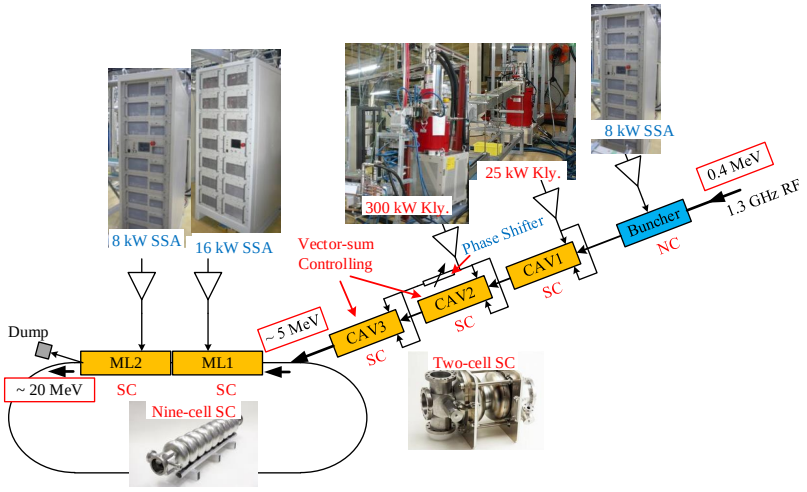

Figure 1: Layout of cERL. The cavities and RF sources are shown in the figure. The energies and accelerating field in the cavities are also marked as well.

frequency noise level. Furthermore, the frequency of 20 kHz exceeds the effective bandwidth of the DOB controller, which is usually less than 5 kHz under FB operation [2].

Active noise control (ANC) technology has been widely used in electroacoustic or electromechanical systems to attenuate the low-frequency noise in situations where other methods are ineffective [5, 6]. In recent years, narrow-band ANC-based control approaches have been successfully applied at facilities such as European X-ray free electron laser (XFEL) and Cornell-BNL ERL test accelerator (CBETA) to reject microphonics with a cavity resonance control system [7, 8, 9]. In these applications, the ANC controller estimates the amplitude and phase of the sinusoidal microphonics detuning and then cancels their effects with feedforward (FF) control. Since both the microphonics and HVPS ripples are reflected by a sum of sinusoidal disturbances in the RF field, especially in the RF phase, this inspires us to extend the narrow-band ANC algorithm to the LLRF field control to reject the HVPS ripples. In this paper, Section 2 briefly introduces the LLRF system. In addition, the measured HVPS ripple effects in CAV1 and CAV2&3 are presented in this section. In Sec. 3, we describe the principle of the narrow-band ANC algorithm; some Matlab-based analysis is presented as well. Section 4 depicts the FPGA implementation of the ANC controller. Section 5 presents

the results of this controller in the cERL beam-commissioning. Furthermore, the comparison of ANC control and DOB control are discussed as well. Finally, in Sec. VI, we present a summary of our work.

2. Suppression of HVPS ripples by LLRF system

The simplified diagram of the digital LLRF system of the cERL is shown in Fig.2 [2, 4]. The 1.3 GHz RF signals from the cavities are down-converted to 10 MHz intermediate frequency (IF) signals. The IF signals are sampled in the next stage at 80 MHz and fed to a micro telecommunications computing architecture (μTCA) FPGA to execute the digital signal processing algorithms. The in-phase and quadrature components (I/Q) are then extracted from the IF signal [10]. The VS signal is calibrated by calculating the superposition of all the cavity pick-up signals. After being filtered by digital low-pass filters, the I/Q components are compared with the reference signal and the I/Q errors are calculated. Then, these I/Q errors are regulated by a PI FB controller. The regulated I/Q signals are added to the FF models. The combined signals are fed to the I/Q modulator to modulate the RF signal from the master oscillator. Finally, the LLRF FB loop is closed by means of a high power RF source, which drives the cavities. Embedded Linux is installed in a Power-PC of the μTCA FPGA board. The experimental physics and industrial control system (EPICS) is installed in the Linux system for communication control, and hence the board acts as an EPICS input/output controller (IOC) [11, 12].

The RF system is subjected to various disturbances. In the cavities of the cERL ML, the dominant disturbance under CW mode operation is microphonics due to the high Q_L of the cavities. In the cavities of the cERL injector, besides microphonics, the HVPS ripple is another main disturbance that deteriorates the RF stability, especially the RF phase stability [4]. The measured HVPS ripples from the oscilloscope is shown in Fig.3(a). A 20 kHz component is observed in the HVPS output of the 25 kW klystron; likewise, a 300 Hz component exists in the 300 kW klystron HVPS. This 20 kHz component is produced by the switching invertor-type power supply. The 300 Hz component is caused because the DC power supply uses a three phase controlled thyristor rectifier. The peak-to-peak voltage fluctuation ($\Delta V_k/V_k$) of the above two components are $\pm 0.05\%$ and $\pm 0.17\%$, respectively. The

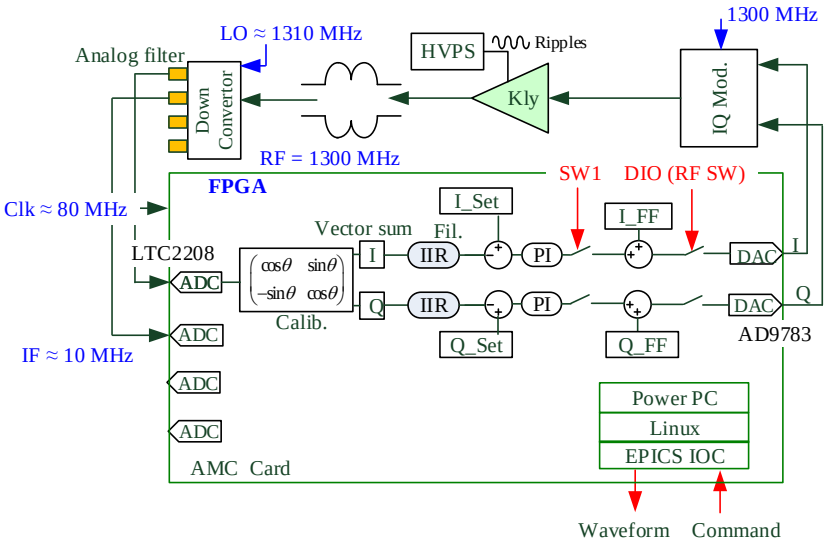

Figure 2: Diagram of the LLRF system in the cERL at KEK. This figure shows the case of individual cavity control in which one klystron drives one cavity. In the case VS control, multiple cavities will be driven by one klystron.

corresponding klystron phase fluctuation $\Delta\theta_{kly}$ is expressed as [13]

$$\Delta\theta_{kly} = D\frac{\Delta V_k}{V_k}, \tag{1}$$

where D represents the voltage fluctuation coefficient for the klystron phase modulation. This coefficient is determined by the klystron cathode voltage V_k and the drift tube length L (the length between the input cavity and output cavity of the klystron). In our case, the value L is approximately 0.48 m for both the klystrons, and the operational V_k is 20 kV for the 25 kW klystron and 35 kV for the 300 kW klystron. According to Ref. [13], the value of D is approximately $13.0°/\frac{\Delta V_k}{V_k}[\%]$ for the 25 kW klystron and $9.7°/\frac{\Delta V_k}{V_k}[\%]$ for the 300 kW klystron. Accordingly, the corresponding phase fluctuations of the 25 kW klystron at 20 kHz and 300 kW klystron at 300 Hz are approximately $\pm 0.65°$ and $\pm 1.65°$, respectively.

Figure 3 (b) shows the measured Fast Fourier Transformation (FFT) analysis of the klystron output phase. The amplitudes of the phase fluctuation of the corresponding components are 0.58°and 1.6° for the 25 kW klystron

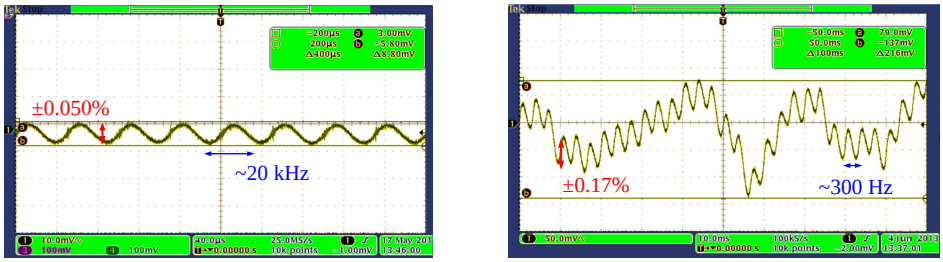

(a)

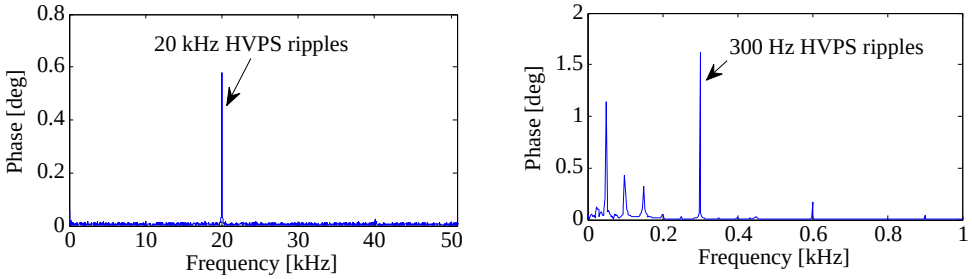

(b)

Figure 3: (a): HVPS ripples measured from oscilloscope. (b) FFT analysis of klystron output phase. The amplitude of the phase modulation is approximate 0.58° at 20 kHz for the 25 kW klystron (left), and 1.6° at 300 Hz for the 300 kW klystron (right).

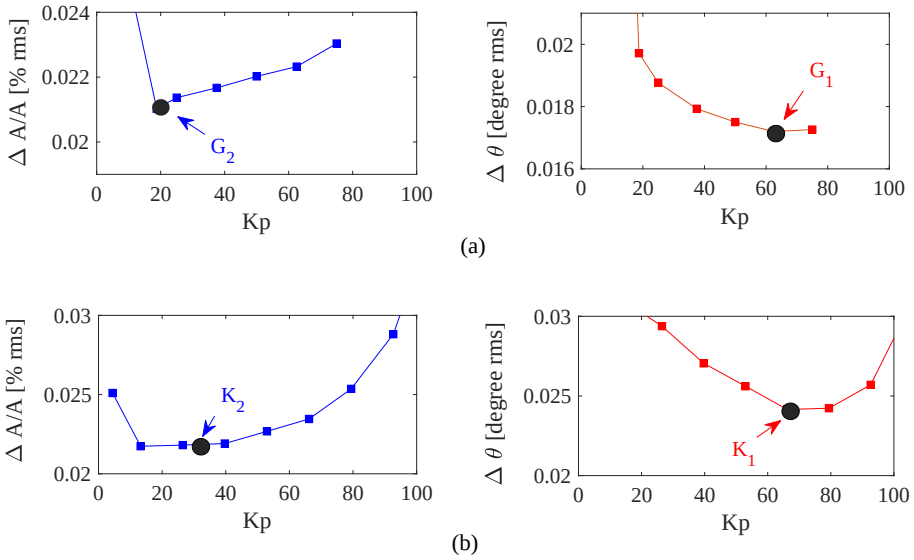

Figure 4: Gain-scanning result for (a): CAV1, (b): CAV2&3 (VS control). The subplots on the left and right indicate the amplitude and phase stabilities, respectively. Before 2014, G_1 and K_1 were determined as the optimal gains according to the phase performance. From 2015 to present, G_2 and K_2 were selected as the operational gain to reduce the RF trips.

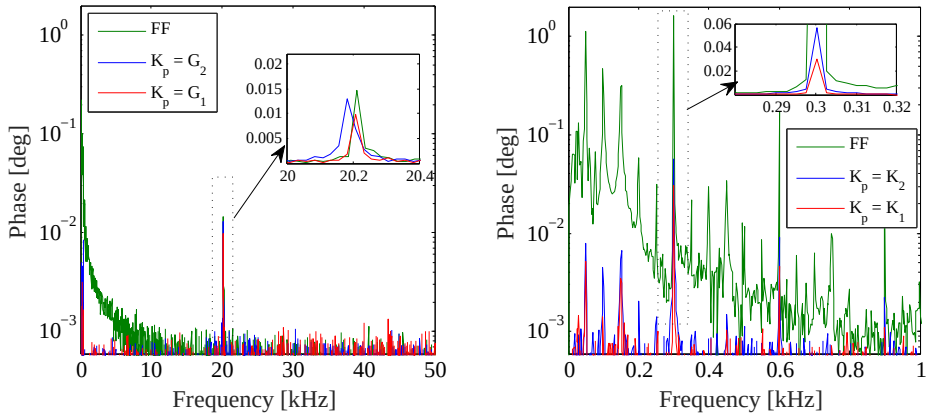

Figure 5: FFT results of cavity phase in the case of FF operation (green), $K_p = G_2$ or K_2 (blue) and $K_p = G_1$ or K_1 (red). The ripple effect always exists in all of these three cases.

and 300 kW kystron, respectively. The results are in good agreement with the value calibrated from Eq.(1).

High FB gains are required to suppress the ripples. To optimize the PI gains in the FB loop, a gain scanning experiment was performed. The optimal gains were determined according to the scanned performance curves. Detailed information about this scanning process was presented in Ref. [14] and Ref. [15]. Under optimal integral gain (K_i), which is approximately 1×10^5 in our case, the amplitude (left) and phase (right) stabilities as functions of proportional gain (K_p) are illustrated in Fig. 4. The optimal gain for phase is usually larger than the optimal gain for amplitude. One possible reason is that disturbance such as microphonics and ripples mainly influence the RF phase. To reject these disturbances in the RF phase, a higher K_p is preferred. However, the high FB gains not only increase the risk of an unstable system but also increase the noise level of the high-frequency components. Before the year 2014, the optimal gains were mainly determined on the basis of phase performance, i.e., we selected G_1 and K_1 as the optimal gains for CAV1 and CAV2&3. However, A few RF trips occurred in our system due to the high LLRF FB gain. These situations forced us to decrease the gain from G_1 and K_1 to G_2 and K_2 after the year 2015. The gain G_2 is selected as the operational gain of CAV1 mainly on the basis of amplitude performance (we can achieve optimal amplitude stability under G_2). The gain $K_2 = 0.5 \cdot K_1$ was determined for the operational gain of CAV2&3 to make compromises between the amplitude stability and phase stability. The RF trips due to the LLRF system were significantly reduced as presented in Ref.[16].

Figure 5 compares the FFT analysis of the cavity phase under FF operation, FB operation with G_2 (or K_2) and FB operation with G_1 (or K_1). It can be clearly seen that the 20 kHz and 300 Hz ripples still exist even under high gains G_1 and K_1. If we continue to increase the gains to higher values, the RF stabilities of both amplitude and phase become worse as shown in Fig. 4.

3. Narrow-band ANC algorithm

ANC control is commonly used in electroacoustic and electromechanical systems to cancel unwanted noise. In this method, an anti-noise signal with the same amplitude but opposite phase is generated by the ANC algorithm, and then noise cancellation is realized with FF method [5, 7, 8, 9]. Usually, an

external reference detector is required to calculate the noise that needs to be canceled. In a special case of narrow band noise (e.g., sinusoidal noise), such as microphonics or HVPS ripples, an internal reference may also be effective. These facts provide a possibility to simplify the design of the system. In European-XFEL, a narrow-band ANC method with an internal reference was applied in the piezo-based resonance control system to reject the low-frequency microphonics noise [7]. In CEBTA, an enhanced version of narrow-band ANC algorithm, with adaptively tunes the control parameters, was successfully implemented to suppress the microphonics detuning [8]. Since both the microponics and HVPS ripples can be seen as a superposition of sinusoidal signals, we were inspired to design a narrow-band ANC-based method to reduce the ripple effects in our system.

Since the ripple effects are mainly concentrated in the RF phase, we only consider the implementation of the ANC algorithm in the phase loop in this paper for simplicity. Generally, one ANC unit cancels only one components. Therefore, for the applications in Ref.[7] and Ref.[8], several ANC unites were combined to suppress the microphonics which includes several components. However, in our case, as shown in Fig. 5, the 20 kHz and 300 Hz ripples are the dominant components for CAV1 and CAV2&3, respectively. This would become more clear by investigating the accumulative phase RMS stability as shown later in Fig.13. Therefore, we need only one ANC controller to cancel the ripple effects.

In principle, the LLRF system is a muti-input muti-output system. Since the Lorentz force detuning effect is not serious due to the CW mode operation, the microphonics detuning is well compensated by the resonance control loop in the cavities of the injector. That is, the cavity is assumed to be operated on-resonance in our system. Under this assumption, the LLRF system for the phase loop control is considered as a single-input single-output system.

Figure 6 shows the simplified model of the ANC control in combination with PI control. If the cavity is operated on resonance, the cavity transfer function $H_{cav}(s)$ is simplified as

$$H_{cav}(s) = \frac{\omega_{0.5}}{s + \omega_{0.5}}, \tag{2}$$

where the parameter $\omega_{0.5}$ represents the cavity half-bandwidth. The transfer function $H_T(s) = e^{-T_d \cdot s}$ represents the loop delay model in the system. In our system, the loop delay T_d is approximately 1 μs. Here, the model H_{PI}

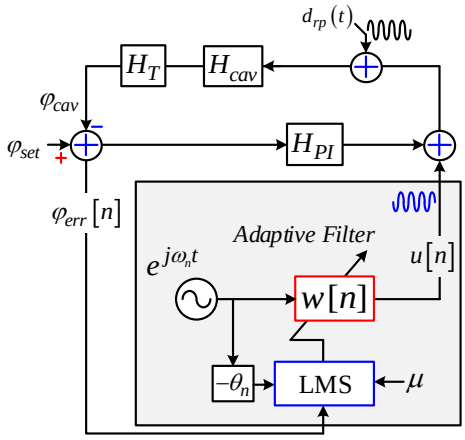

Figure 6: Phase loop model of ANC-based controller in combination with PI controller. The ANC controller is indicated by the grey block. The main components of the ANC controller include an adaptive filter $w(n)$ (indicated by red block) and an LMS algorithm (indicated by blue block).

represents the PI FB controller. It should be noted that in this paper, the PI controller is defined by its continuous-time form

$$H_{PI}(s) = K_p + \frac{K_i}{s}. \tag{3}$$

The HVPS ripples at a specified frequency are expressed by a sinusoidal signal $d_{rp}(t)$ with a frequency ω_{rp}, amplitude A_{rp}, and phase ϕ_{rp}:

$$d_{rp}(t) = A_{rp} sin(\omega_{rp} t + \phi_{rp}). \tag{4}$$

The ANC controller is indicated by the grey block in Fig. 6. The oscillator $e^{j\omega_n t}$ provides a pair of orthogonal signals $sin(\omega_n t)$ and $cos(\omega_n t)$, which are used as reference inputs for an adaptive filter $w(n)$ with filter weights w_1 and w_2. The value of ω_n is selected based on the actual ripple frequency ω_{rp} (e.g., 20 kHz and 300 Hz in our case). The orthogonal references are then weighted and summed to produce the canceling signal $u(t)$

$$u(t) = w_1 \cdot sin(\omega_n t) + w_2 \cdot cos(\omega_n t). \tag{5}$$

By using the samples $n = t/\Delta t$ to replace the parameter t, where Δt is the sampling duration, the canceling signal $u(t)$ becomes

$$u[n] = w_1[n] \cdot sin[\omega_n \Delta t \cdot n] + w_2[n] \cdot cos[\omega_n \Delta t \cdot n]. \tag{6}$$

The adaptive weights $w_1[n]$ and $w_2[n]$ are updated by the least mean square (LMS) algorithm as follows:

$$w_1[n+1] = w_1[n] + \mu \cdot \varphi_{err} \cdot sin[\omega_n \Delta t \cdot n - \theta_n]\,. \tag{7}$$

$$w_2[n+1] = w_2[n] + \mu \cdot \varphi_{err} \cdot cos[\omega_n \Delta t \cdot n - \theta_n]\,. \tag{8}$$

Here μ is the step size parameter of the LMS algorithm, and φ_{err} represents the cavity phase error, which is the difference between the cavity phase φ_{cav} and phase set value φ_{set}. The parameter θ_n is the nominal phase response of the original system (which is the system without ANC controller) at the frequency ω_n. Here, we use θ_n to compensate for the phase shift in the original system. Assume that the actual phase response at ω_n for the original system is θ_p. Then, the stability condition is satisfied if the difference between θ_p and θ_n is less than 90° [5, 7, 8, 9]. The value of ω_n can be easily predicted by the bode diagram. Since a ±90° error of ω_n is acceptable, it is possible to optimize ω_n experimentally.

The steady state transfer function of this ANC controller from the error $\varphi_{err}[n]$ to ANC output $u[n]$ is [7, 8, 6]

$$H_{anc}(z) = \mu \cdot \frac{cos(\omega_n \Delta t - \theta_n)z - cos(\theta_n)}{z^2 - 2cos(\omega_n \Delta t)z + 1}\,. \tag{9}$$

Figure 7 compares the closed loop transfer function from d_{rp} to the cavity phase φ_{cav} in the case of PI individual control and "PI+ANC" control. In the steady state, the transfer function of PI+ANC control is given by

$$H_{d_{rp}\to\varphi_{cav}} = \frac{H_{cav} \cdot H_T}{1 + (H_{PI} + H_{anc}) \cdot H_{cav} \cdot H_T}\,. \tag{10}$$

On the other hand, the transfer function of PI individual control is given by

$$H_{d_{rp}\to\varphi_{cav}} = \frac{H_{cav} \cdot H_T}{1 + H_{PI} \cdot H_{cav} \cdot H_T}\,. \tag{11}$$

Here, the parameters in the cavity model H_{cav} are selected based on CAV1 ($Q_L \approx 1.2 \times 10^6$). The loop delay T_d is supposed to be 1 μs as mentioned above. The FB gain for K_p is selected as G_2. The parameter ω_n is set to 20 kHz to suppress the ripples. As shown in Fig. 7, the ANC algorithm performs like a notch filter and the center of the notch filter is defined by ω_n.

Figure 8 shows the influence of μ and θ_n. The parameter μ determines the bandwidth of the notch. The parameter θ_n may lead to an asymmetric magnitude response. Regardless of the value of θ_n, there is a notch in the frequency of ω_n.

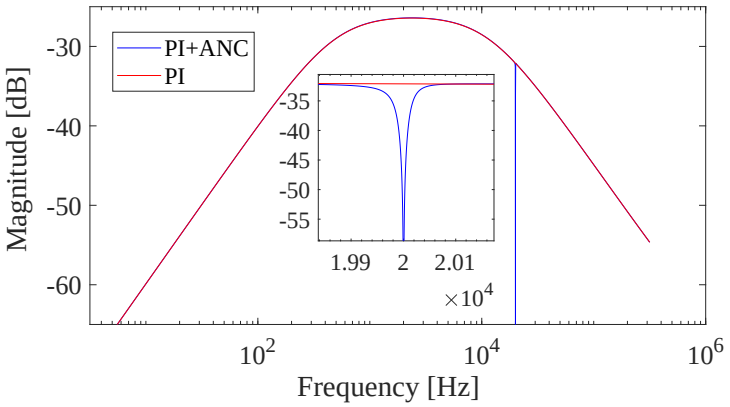

Figure 7: Comparison of the closed-loop transfer function from d_{rp} to φ_{cav} in the case of PI individual control (red) and "PI+ANC" control (blue). The ANC algorithm acts like a notch filter with the notch center defined by ω_n.

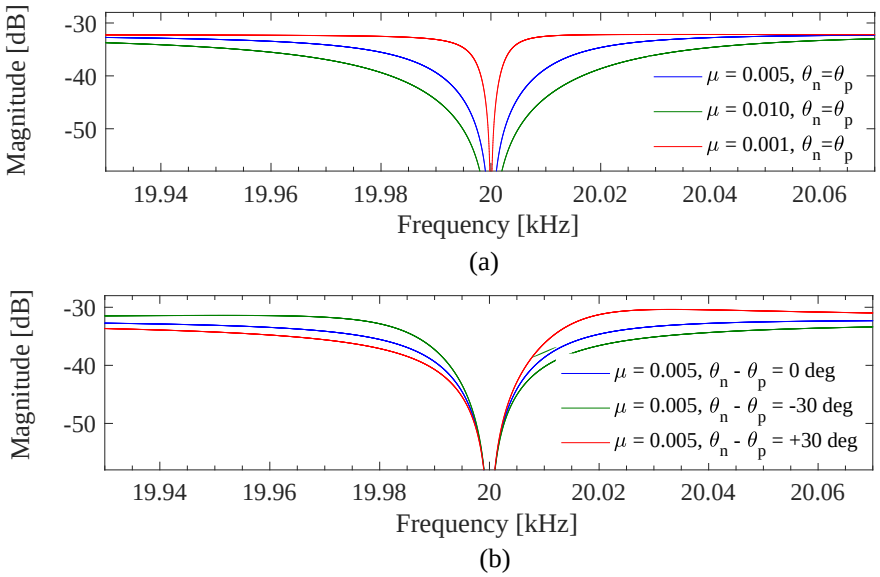

Figure 8: Magnitude of the closed loop transfer function in terms of different ANC parameters (a) μ and (b) θ_n. The parameter μ regulates the effective bandwidth of the ANC controller, whereas the parameter θ_n affects the symmetry of the magnitude response.

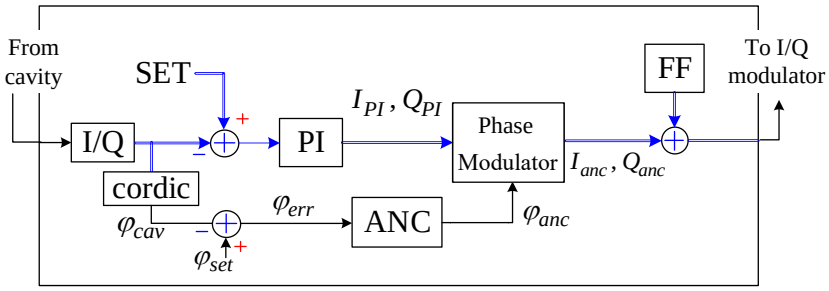

Figure 9: Overall algorithm of "PI+ANC" control. The "Phase Modulator" model is used to phase modulate the PI controller output with φ_{anc}. The I/Q signals path is indicated by blue color.

4. FPGA implementation of the ANC controller

Since the structure of the narrow-band ANC algorithm is relatively simple, it can be implemented inside the FPGA in real-time. The combination of the PI controller and the ANC controller is shown in Fig. 9. The cavity phase φ_{cav} is extracted from the cavity I/Q signal by the coordinate rotation digital computer (CORDIC) algorithm. The CORDIC algorithm can be used to realize a mutual transformation from the rectangular coordinate (e.g., I/Q) to the polar coordinate system (e.g., amplitude and phase). The cavity phase error φ_{err} is then obtained by calculating the difference between φ_{cav} and the phase set value φ_{set}; φ_{err} is regulated by the ANC controller. The processed phase signal φ_{anc} is used to modulate the PI controller output I_{PI} and Q_{PI} using the "Phase Modulator" model. The structure of this model will be discussed in the following paper.

Figure 10 shows the structure of the ANC controller in FPGA. The internal reference signals $sin[\omega_n \Delta t \cdot n]$ and $cos[\omega_n \Delta t \cdot n]$ are generated by CORDIC-based numerically controlled oscillator. An additional phase offset θ_n is introduced to compensate for the phase shift in the system as discussed in Sec. 3. The regulated reference signals are then sent to the LMS algorithm to update the filter weights w_1 and w_2. The update rules are given in (7) and (8) in Sec. 3. The ANC output phase is then calculated by the adaptive filter using (6). Here, the "limit" model is used to keep the ANC output in a bounded range in order to protect the system under abnormal cases (e.g. the utilization of unreasonable θ_n or μ).

The PI output signal need to be phase modulated by φ_{anc}. Suppose the

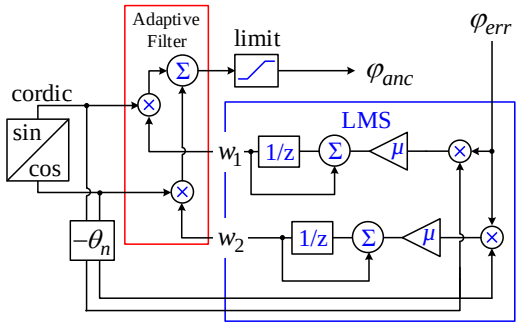

Figure 10: Structure of ANC controller in FPGA. The adaptive filter and the LMS algorithm are indicated by the the red and blue blocks, respectively.

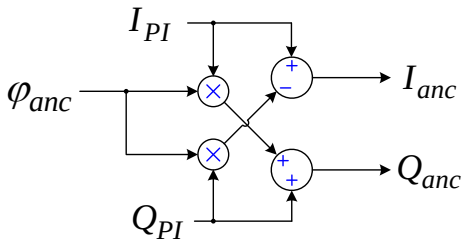

Figure 11: Structure of the phase modulator model in FPGA.

I/Q output of the PI controller is defined as

$$\begin{cases} I_{PI} &= A cos(\alpha)\,, \\ Q_{PI} &= A sin(\alpha)\,. \end{cases} \tag{12}$$

Then, the corresponding I/Q signal that phase modulated by φ_{anc} is given by

$$\begin{cases} I_{anc} &= A cos(\alpha + \varphi_{anc}) = I_{PI} \cdot cos(\varphi_{anc}) - Q_{PI} \cdot sin(\varphi_{anc})\,, \\ Q_{anc} &= A sin(\alpha + \varphi_{anc}) = I_{PI} \cdot sin(\varphi_{anc}) + Q_{PI} \cdot cos(\varphi_{anc})\,. \end{cases} \tag{13}$$

It should be noted that, the value of φ_{anc} for ripples compensation is usually less than 2 degrees (actually, it is approximately 0.6 degree for CAV1 and 1.7 degrees for CAV2&3); that means, we have $cos(\varphi_{anc}) \approx 1$ and $sin(\varphi_{anc}) \approx \varphi_{anc}$. Therefore, similar to that in Ref. [17], Eq. (13) is simplified into

$$\begin{cases} I_{anc} &\approx I_{PI} - Q_{PI} \cdot \varphi_{anc}\,, \\ Q_{anc} &\approx Q_{PI} + I_{PI} \cdot \varphi_{anc}\,. \end{cases} \tag{14}$$

The structure of the phase modulator model ("Phase Modulator" in Fig. 9) in FPGA is illustrated in Fig. 11.

Finally, we summarize the utilization of the FPGA resources of the ANC controller including the phase modulator model (Fig. 11) in Table 1. The ANC control occupies a few registers due to the implementation of the CORDIC algorithms.

Table 1: FPGA resource utilization of ANC controller

Block	Available	ANC controller	[%]
Register	44800	1471	3.3%
DSP48Es	128	8	6.3%
Block RAM	148	0	0%

5. Results and Discussion

To validate the ANC control, we integrated the ANC controller into the PI feedback loops in the μTCA-based LLRF systems of CAV1 and CAV2&3. Table 2 lists the main parameters of the cavities and LLRF systems.

Table 2: LLRF and cavity parameters of CAV1, CAV2, and CAV3 in the cERL injector

Cavity	CAV1	CAV2	CAV3
Cavity Field (E_{acc})	~ 5 MV/m	~ 5 MV/m	~ 5 MV/m
Beam Phase (Φ_b)	0°	0°	0°
Loaded Q (Q_L)	1.2×10^6	5.7×10^5	4.8×10^5
Cavity Bandwidth ($\omega_{0.5}$)	540 Hz	1120 Hz	1350 Hz
Time Delay (T_d)	1 μs	1 μs	1 μs
Power Source	25 kW klystron	300 kW klystron (VS ctrl.)	
PI Gains (K_p, K_i)	(G_2, 0.6×10^5)	(K_2, 0.7×10^5)	
Dominant Ripples	20 kHz	300 Hz	

To compare the PI individual control and "PI+ANC" control, we first operate the LLRF system with PI individual control on CAV1. As shown in Fig. 12 (a), the red curves give the amplitude and phase responses and theirs corresponding FFT analysis of CAV1 under PI individual control. Here, the FB gain K_p was set to G_2. As expected, the 20 kHz ripple components were easily found in the FFT analysis of the cavity phase. In the next step, after activating the ANC control (indicated by the blue curves in Fig. 12) and keeping the PI control in the same condition as before, the 20 kHz component in the cavity phase was well suppressed as shown in the FFT analysis of Fig. 12 (a). For CAV2&3, a similar result can be found in Fig. 12 (b); the 300 Hz component in the VS phase of CAV2 and CAV3 is almost canceled out by the ANC control.

Comparisons of the cumulative RMS stabilities of CAV1 and CAV2&3 under PI individual control (red) and "PI+ANC" control (blue) are shown in Fig. 13 (a) and Fig. 13(b), respectively. From the amplitude cumulative RMS stability curves (left side) in Fig. 13, it can be seen that the contribution of the 20 kHz ripple to the overall amplitude stability is almost negligible for CAV1. The contribution of the 300 Hz ripple for CAV2&3 is about 8% in both the control approaches. In principle, if we apply the presented ANC method in both amplitude and phase loops (or I/Q loops), the ripple effects in the amplitude can be rejected. In our application, since the ripple effects in

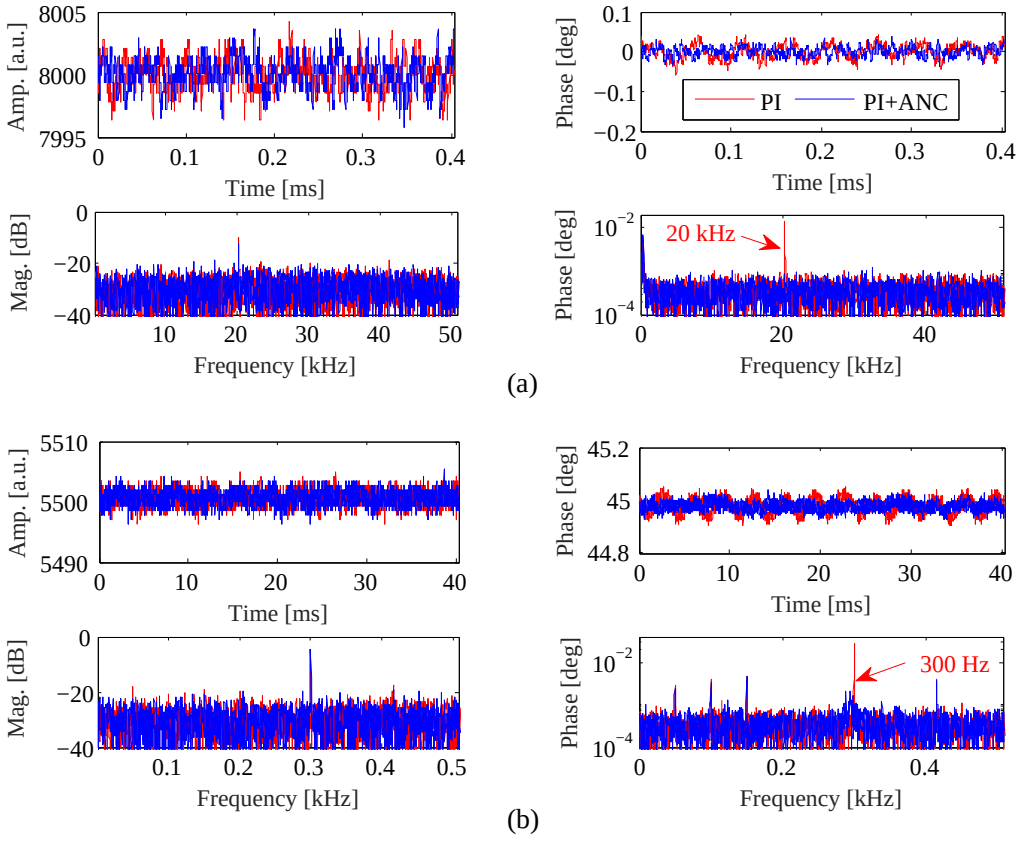

Figure 12: PI individual control (red) vs "PI+ANC" control (blue) in 2018. The amplitude and phase of the cavity field, and the corresponding FFT analysis are plotted. From top to bottom: (a) CAV1, $K_p = G_2$ and (b) VS of CAV2 and CAV3, $K_p = K_2$.

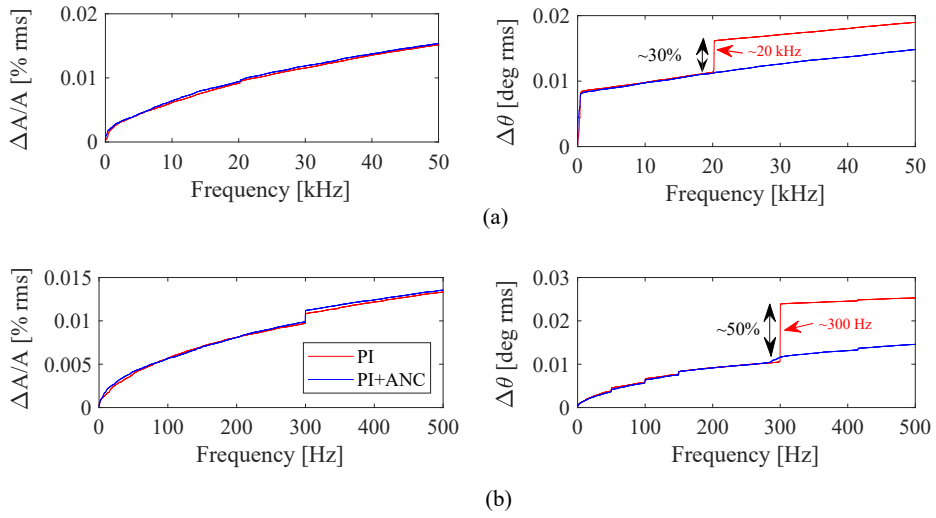

Figure 13: Cumulative RMS amplitude (left) and phase (right) stabilities of (a) CAV1 and (b) VS of CAV2 and CAV3 under PI individual control (red) and "PI+ANC" control (blue) in 2018. The contribution of the 20 kHz and 300 Hz ripples to the overall phase RMS stability are 30% and 50%, respectively.

the amplitude are not as serious as those in the phase, we only implemented the ANC algorithm in the phase loop to save FPGA resources. Therefore, there is no improvement in amplitude performance. In all the cavities, the ripple components significantly influence the phase stability. For CAV1, the contribution of the 20 kHz ripple effects on the RMS phase stability is about 30% of the total stability. In the case of CAV2&3, the contribution of the 300 Hz ripple to the total stability is about 50%. The phase performance is significantly improved after activating the ANC control. It should be noted that the ANC algorithm is only effective for the frequency of interest (defined by ω_n in the ANC controller). Other components such as 50 Hz and 150 Hz in CAV2&3 are not sensitive to the ANC controller.

Table 3 summarizes the improvements of ANC control in comparison with PI individual control. The phase performance in all of these cases are improved by the ANC technique.

It is interesting to compare the ANC control with DOB control, which is another advanced control method used in the cERL commissioning [2]. The basic architecture of the DOB control in combination with PI control is

Table 3: Performance of ANC control for the suppression of ripples during the cERL beam commissioning in 2018.

Cavity	K_p	Method	RF field stability	
			$\Delta A/A$ [% rms]	$\Delta\theta$ [° rms]
CAV1	G_2	PI	0.015%	0.019°
		PI+ANC	0.015%	0.014°
	G_1	PI	0.016%	0.016°
		PI+ANC	0.016%	0.013°
CAV2&3 Vector-sum	K_2	PI	0.014%	0.025°
		PI+ANC	0.014%	0.014°

illustrated in Fig. 14. The definitions of the models H_{cav}, H_T and H_{PI} are the same as those in Fig. 6. The model H_n^{-1} is the inverse transfer function of the nominal cavity model H_n. A low-pass Q filter is connected with H_n^{-1} to make the overall combination $Q \cdot H_n^{-1}$ casual. By using H_n^{-1}, it is possible to estimate the nominal system drive signal $\hat{u}$. If the model H_n is sufficiently precise, which means that $H_n \approx H_{cav}$, the signal $\hat{u}$ is approximately equal to the actual drive signal u. The signal u_f is the filtered drive signal but without disturbances. The model z^{-L} is introduced here to compensate for the loop delay T_d. Therefore, we can obtain the disturbance estimation $\hat{d}$ by calculating the difference between $\hat{u}$ and u_f. Finally, we remove $\hat{d}$ from the drive signal to realize the disturbance rejection. In DOB control, the low-pass Q filter determines the effective bandwidth of the controller [2, 18]. Detailed information about this DOB-based method can be found in Ref.[2].

Figure 15 compares the cumulative RMS stabilities of CAV1 and CAV2&3 under PI individual control (red) and "PI+DOB" control (blue). For consistency, the gain K_p was set to G_2 and K_2 for CAV1 and CAV2&3, respectively. The cavity fields are approximately 3 MV/m for all of the 3 cavities. To evaluate whether we can remove the 20 kHz ripple by DOB control, we increase the bandwidth of the Q filter in the DOB control to more than 5 kHz, which is almost the highest value that can be achieved under the FB operation [2]. Since the 20 kHz ripples component is still beyond the effective bandwidth of DOB control, it is clearly seen in Fig. 15(a) that there is no improvement

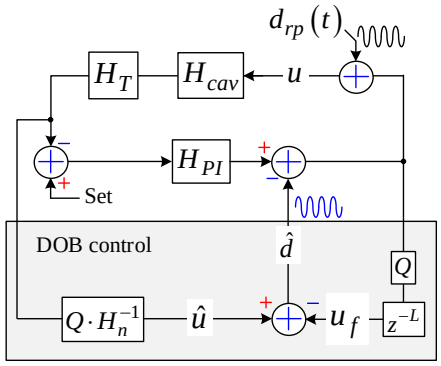

Figure 14: Simplified architecture of DOB control in comparison with PI control. The DOB controller is indicated by the grey block. The disturbance d_{rp} can be estimated by the controller output $\hat{d}$. The effective bandwidth of the controller is determined by the lowpass Q filter.

in the phase performance at 20 kHz. For the low-frequency components of less than several hundreds hertz, the phase performance is improved by DOB control. For the frequency range from 1 kHz to 20 kHz, unfortunately, the DOB control deteriorates the phase stability. The possible reason is that the non-optimal bandwidth of the Q filter was chosen. For CAV2&3, we selected a 2 kHz Q filter for the DOB control to remove the 300 Hz component as shown in Fig. 15(b). In contrast to ANC control, the DOB control is effective not only for 300 Hz but also for other components such as 50 Hz and 150 Hz. Since the dominant 300 Hz ripple effects are rejected, the phase stability of CAV2&3 is improved from 0.026° rms to 0.015° rms by using the DOB control method. The result is comparable with that of the ANC controller (see Table 3).

On comparing of these two controllers, it can be seen that the DOB control is valid in the low-frequency range (e.g., DC to several kHz), but the effective bandwidth is limited by the stability requirements. For better performance, a system model is usually required in this control method [2, 18]. The ANC control is effective for the frequency components of interest with an infinite loop gain. Furthermore, we only need limited phase information of the transfer function for the specified frequency, and a tolerance of up to ±90° errors is acceptable in theory.

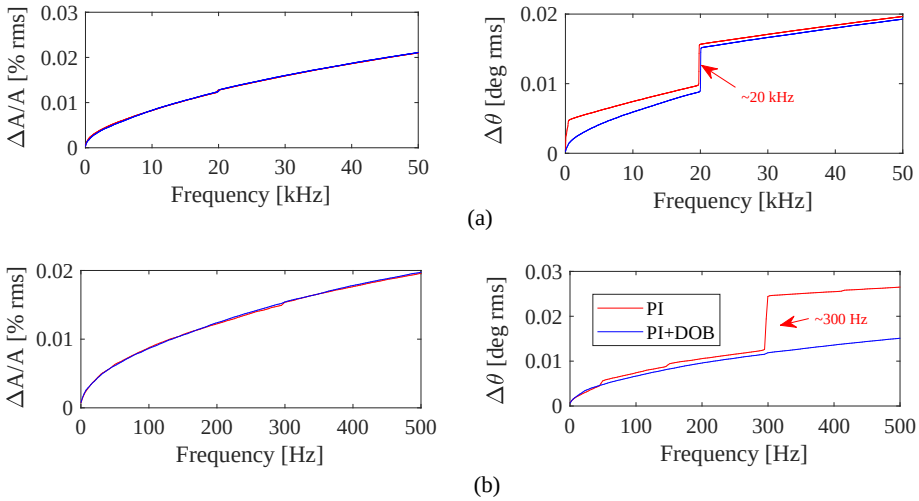

Figure 15: Cumulative RMS amplitude (left) and phase (right) stabilities of (a) CAV1 and (b) VS of CAV2 and CAV3 under PI individual control (red) and "PI+DOB" control (blue) in 2015.

In the current ANC controller, the parameters such as θ_n, and ω_n were kept constant during the operation. However, after a long-term operation, these parameters may vary as the environment changes (e.g., temperature drifts). As future work, those parameters in the ANC controller can be adapted with the LMS algorithm [8]. In addition, we also plan to apply the ANC technique in the resonance control system of the SC cavities in the cERL ML.

6. Summary

ANC control cancels the disturbances by generating an anti-noise signal with equal amplitude but opposite phase. In European-XFEL and CBETA, ANC-based methods have been successfully applied to cancel the microphonics detuning in the SC cavity with piezo tuner.

In the injector of the KEK-cERL, HVPS ripples of 20 kHz and 300 Hz deteriorate the phase performance of the LLRF systems. The high-gain PI control could not achieve the desired level of ripples suppression. Inspired by the experience of European-XFEL and CBETA, we have integrated the

ANC-based algorithm in our LLRF system to damp the ripple components in the RF phase. We demonstrated the effectiveness of this ANC method by successfully canceling out the RF phase ripples during the cERL beam commissioning. In addition, we compared the performance of the ANC method with the DOB-based method. The DOB control method is a model-based method, which is effective in the low-frequency domain with an effective bandwidth (usually less than several kHz) that is limited by the stability requirement. In contrast, the ANC control is efficient only for the frequency component of interest, and it is applicable with very limited information about the system model (i.e., correct θ_n).

References

[1] M. Akemoto et al., Construction and commissioning of compact energy-recovery linac at KEK, Nucl. Instrum. Methods Phys. Res., Sect. A 877 (2018) 197-219.

[2] F. Qiu, S. Michizono, T. Miura, T. Matsumoto, M. Omet, and B. W. Sigit, Application of disturbance observer-based control in low-level radio-frequency system in a compact energy recovery linac at KEK, Phys. Rev. ST Accel. Beams 18 (2015) p. 092801

[3] M. Satoh et al., Mechanical vibration search of compact ERL main linac superconducting cavities in cryomodule, in: Proc. 5th International Particle Accelerator Conference, IPAC14, Dresden, Germany, 2014, 2531-2533

[4] T. Miura et al., Performance of rf systems for compactERL Injector at KEK, in: Proc. 53th ICFA Advanced Beam Dynamics Workshop on Energy Recovery Linacs, ERL-2013, Novosibirsk, Russia, 2013, p. 58.

[5] S. M. Kuo and D. R. Morgan, Active noise control: A tutorial review, Proc. IEEE 87 (1999) 943-973.

[6] S. M. Kuo and M. Ji, Passband disturbance reduction in periodic active noise control systems, IEEE Trans. Speech Audio Process., vol. 4, no. 2, (1996) 96103

[7] R. Rybaniec et al., FPGA-based rf and piezocontrollers for SRF cavities in cw mode, IEEE Trans. Nucl. Sci. 64, (2017) 1382-1388.

[8] N. Banerjee et al., Active suppression of microphonics detuning in high QL cavities, Phys. Rev. Accelerator and. Beams 22 (2019) p. 052002 .

[9] T. H. Kandil et al., Adaptive feedforward cancellation of sinusoidal disturbances in superconducting rf cavities, Nucl. Instrum. Methods Phys. Res., Sect. A 550 (2005) 514-520.

[10] T. Schilcher, RF application in digital signal processing, in: Proc. CERN Accelerator School on Digital Signal Processing, CAS2007, Sigtuna, Sweden, 2007 p. 249.

[11] J. Odagiri, Fully embedded Epics-based Control of Low Level RF system for SuperKEKB, in: 1st International Particle Accelerator Conference, IPAC10, Kyoto, Japan, 2010, 2686-2688

[12] F. Qiu et al., Development of MicroTCA-based Low-level Radio Frequency Control Systems for cERL and STF. in: Proc. 12th Int. Workshop on Emerging Technologies and Scientific Facilities Controls (PCaPAC2018), Hsinchu, Taiwan, 2018, 124-126.

[13] M. Hara et al., A ripple effect of a klystron power supplyon synchrotron oscillation, Part. Accel. 59 (1998) 143-156.

[14] F. Qiu, et al., Feedback optimization in MicroTCA-based LLRF systems, in: Proc. 19th IEEE-NPSS Real Time Conference, Nara, Japan, 2014.

[15] F. Qiu et al., Performance of the digital LLRF system at the cERL, in: Proc. 5th International Particle Accelerator Conference, Dresden, Germany,2014 pp. 2447-2449

[16] K. Umemori et al., Long-term Operation Experience with Beams in Compact ERL Cryomodules, in: Proc. 18th International Conference on RF Superconductivity (SRF2017), Lanzhou, China, 2017 pp. 736-740.

[17] F. Qiu, S. Michizono, T. Miura, T. Matsumoto, N. Liu, and S. B. Wibowo, Real-time cavity simulator-based low-level radio frequency test bench and applications for accelerators, Phys. Rev. Accel. Beams 21 (2018) p. 032003

[18] T. Umeno and Y. Hori, Robust speed control of dc servomotors using modern two degrees-of-freedom controller design, IEEE Trans. Indust. Electron. 38 (1991) 363-369